Polymer Chemistry

ROYAL SOCIETY OF CHEMISTRY

PAPER

View Article Online
View Journal | View Issue

Cite this: *Polym. Chem.*, 2025, **16**, 4341

Synthesis and solution self-assembly of poly(benzotriazole)-*b*-poly(alkyl methacrylate)s

Hilary D. Fokwa,† Li Ji,† Fu-Sheng Wang, Erin C. Krist, Stephanie S. DeLancey, Alessandra Mandala Kol, Megan N. Jackson and Aleksandr V. Zhukhovitskiy *

Received 2nd August 2025,
Accepted 26th August 2025

DOI: 10.1039/d5py00773a

rsc.li/polymers

Conjugated polymers (CPs) constitute a class of optoelectronic materials with a broad range of applications including sensors, photovoltaics, and theranostics. Morphology is a critical factor that governs optoelectronic performance, and solution-based assembly of CPs is a powerful way to control it. However, among CPs, solution self-assembly of electron-deficient CPs remains underexplored. Herein, we have prepared *via* atom transfer radical polymerization and Suzuki catalyst-transfer polymerization a library of poly(benzotriazole)-*b*-poly(alkyl methacrylate)s (**PBTZ-*b*-PRMA**s) with narrow molecular weight distribution (1.04–1.14) and spanning molecular weights of 10.8 to 57.0 kg mol^{-1}. We studied the self-assembly of the rod-coil block copolymers in tetrahydrofuran/hexane and tetrahydrofuran/ethyl acetate mixtures and found that changing the volumes of the two blocks in PBTZ-*b*-PRMAs led to an assortment of morphologies, including toroids, lamellae, and discrete nanofibers.

Introduction

Since the seminal reports by MacDiarmid, Heeger, Shirakawa, and coworkers in the 1970s,[1,2] π-conjugated polymers (CPs) have been recognized as valuable materials for the realization of optoelectronic devices, sensors, and theranostic tools.[3–8] One of the ways to tune the optoelectronic properties of CPs is through their solution-based self-assembly into different morphologies.[9–11] One of the most powerful methods to access CP nanostructures has been *via* the self-assembly of rod-coil block copolymers (BCPs), where the rod block is a CP, while the coil block is typically not. Most of these assemblies have been focused on electron-rich CPs such as poly(thiophene)s and poly(fluorene)s.[11–14] This limited scope is attributed to the fact that electron-deficient CPs remain difficult to synthesize, and accessing their block copolymers is even more challenging. To the best of our knowledge, the synthesis and self-assembly of rod-coil block copolymers of electron-deficient CPs have not yet been reported; yet, we hypothesize that trends in the solution self-assembly of such copolymers would diverge from their electron-rich counterparts due to a diminished spatial extent of π-electron density and altered π–π stacking configurations.[15] To address the above limitations, we set out to explore the synthesis of poly(benzotriazole)-*b*-poly(alkyl methacrylate) copolymers (**PBTZ-*b*-PRMA**s) and their solution-based self-assembly (Fig. 1). This choice of BCP composition is motivated by the availability of controlled approaches for the synthesis of each block,[16–22] the utility of PBTZs in polymer electronics,[23–25] and the tunability of the PRMA solubility as a function of the alkyl substituent "*R*".[20,26]

Results and discussion

Synthesis of diblock copolymers

Key to the synthesis of the target BCPs is the design of a modular dual initiator (**init**, Fig. 2), which enables atom transfer radical polymerization (ATRP)[20,26,27] of methacrylates followed by Suzuki catalyst-transfer polymerization (SCTP)[17,18] of a benzotriazole derivative to afford a library of rod-coil BCPs. We opted to utilize ATRP because it has a large monomer scope and affords well-defined "coil" polymers with narrow

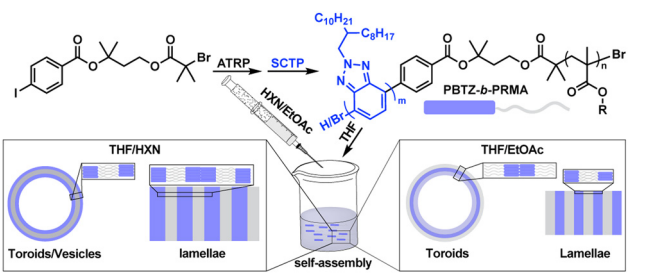

Fig. 1 Generic reaction scheme for the synthesis of **PBTZ-*b*-PRMA**s *via* ATRP and SCTP, followed by their solution-based self-assembly.

Department of Chemistry, University of North Carolina at Chapel Hill, Chapel Hill, North Carolina 27599, USA. E-mail: alexzhuk@email.unc.edu
†Authors contributed equally to work.

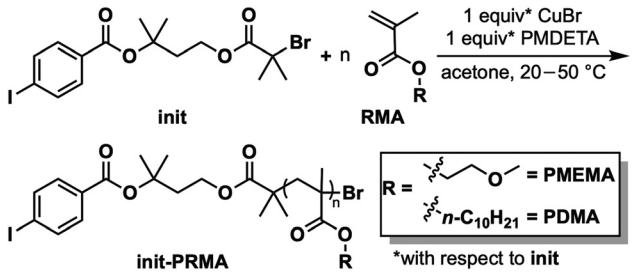

Fig. 2 Synthesis of macroinitiator **init-PRMA**.

Table 1 Characterization of macroinitiators **init-PRMA**

Entry	**init-PRMA**	$M_{n,NMR}$ [a] (kg mol^{-1})	$M_{n,GPC}$ [b] (kg mol^{-1})	$Đ$ [c]
1	**init-PMEMA^{5k}**	5.24	4.81	1.18
2	**init-PMEMA^{7k}**	7.26	8.53	1.26
3	**init-PMEMA^{22k}**	22.1	29.3	1.10
4	**init-PMEMA^{27k}**	27.3	30.4	1.11
5	**init-PDMA^{10k}**	10.4	13.2	1.07
6	**init-PDMA^{32k}**	31.5	23.3	1.18

[a] Number-average molecular weight determined (M_n) *via* ^{1}H nuclear magnetic resonance spectroscopy. [b] M_n determined *via* GPC-MALS ($M_{n,\ GPC}$) in THF at 35 °C. [c] Dispersity ($Đ$) was determined *via* GPC-MALS in THF at 35 °C.

dispersity ($Đ$); meanwhile, we selected SCTP for the conjugated rod block because, among the known approaches to access PBTZ, it offers the greatest control over chain-end fidelity and $Đ$, which are both desirable in the context of BCP synthesis and self-assembly. Although bifunctional initiators have been used to access poly(thiophene)-based rod-coil BCPs, they remain unexplored for the synthesis of electron-deficient conjugated rod-coil BCPs.[13,28,29]

The choice of ATRP for the PRMA block compelled us to add the bromoisobutyryl (BiB) group on one side of the dual initiator. The other terminus of the dual initiator posed more of a design challenge. Typically, SCTP is initiated *via* oxidative addition of (RuPhos)Pd to 4-iodobenzonitrile, presumably to ensure that this step is rapid and quantitative. The nitrile group was not ideal for us however: the need to link the SCTP initiator fragment to the ATRP one would require yet another substituent to be installed onto the benzene ring, complicating the synthesis. As a compromise, and inspired by the work of Itami, Yagi, and coworkers,[30] we replaced the nitrile with an ester group, which we hypothesized would be sufficiently electron-withdrawing to provide for rapid oxidative addition, while also linking the aryl group to the ATRP initiator moiety. Notably, standard SCTP conditions include aqueous alkaline media, which could hydrolyze the ester group. To mitigate this issue, we designed both ester groups of **init** to be sterically hindered, and ATRP of methacrylate rather than acrylate monomers was also chosen for this reason.[31] The synthesis of **init** was accomplished expediently through two esterification reactions starting with the commercial 3-methylbutan-1,3-diol (Scheme S1).

With self-assembly in mind, for the coil block we selected 2-methoxyethyl methacrylate (MEMA) and *n*-decyl methacrylate (DMA) monomers: the former offers solubility in polar solvents,[32] which we have observed to be poor solvents for PBTZs; as a counterpoint, the latter was expected to have much more subtle solubility differences to PBTZ. With the dual initiator in hand, we utilized ATRP to first prepare a small library of macroinitiators (**init-PMEMA** and **init-PDMA**) with a narrow molecular weight distribution and number-average molecular weights (M_n) ranging from 5.24 to 31.5 kg mol^{-1}, determined *via* ^{1}H nuclear magnetic resonance (NMR) spectroscopy as well as gel permeation chromatography with multi-angle light scattering (GPC-MALS) (Table 1).

Next, we explored the chain extension of these macroinitiators to grow the PBTZ block. We chose to use the 3rd-generation (RuPhos)Pd precatalyst because it had been reported for the block copolymerization of PBTZ with the ability to control the polymer molecular weights and maintain low $Đ$.[17,33] We were also inspired by Suzuki–Miyaura cross-coupling conditions advanced by Denmark and coworkers[34]—namely, using KOTMS as the base in toluene—because these conditions were successfully employed by Shi, Marks, and Huang to achieve Suzuki–Miyaura polycondensations.[17,35] Notably, we found that the addition of water (1×10^4 equiv. relative to macroinitiator) was critical to enact the polymerization. We opted for 7-bromo-2-(2-octyldodecyl)-2*H*-benzo[*d*][1,2,3]triazol-4-yl boronate (**BTZ^{2OD}**, Fig. 3A) as the monomer with the 2-octyldodecyl side-chain to enhance the solubility of PBTZ during polymerization and self-assembly. The boronic acid was masked as an *N*-coordinated boronate, which had been shown to slow the rate of hydrolysis and prevent protodeboronation and homocoupling.[18,36] Typically, the SCTP reactions were monitored *via* ^{1}H NMR spectroscopy (Fig. 3B); monomer consumption reached completion after 0.5–2.5 hours, at which point the reactions were quenched with 1 M HCl$_{(aq)}$. The SCTP reactions were also monitored *via* GPC-MALS, which revealed a shift of the polymer peak to progressively lower retention times over the course of the reaction (Fig. 3C); these data were in line with chain extension of the macroinitiator.

Recycling preparative GPC (prep-GPC) was used to purify the diblock copolymers, and diffusion ordered spectroscopy (DOSY) of the purified materials displayed an identical diffusion coefficient (1.4×10^{-6} cm^2 s^{-1}) for resonances corresponding to both blocks (Fig. S1–S2), which supports the notion that the two blocks are linked. ^{1}H NMR spectroscopy also allowed us to calculate the degree of polymerization (DP) of each block and the overall M_n of the purified polymers using the initiator benzene protons as the reference, and these numbers, ranging from 10.8 to 57.0 kg mol^{-1}, were generally on par with those determined through GPC-MALS (Table 2). As the DP of the PBTZ block increases, the biphasic reaction conditions lead to polymer aggregation, which we hypothesize halts further chain growth. Decreasing the concentration of

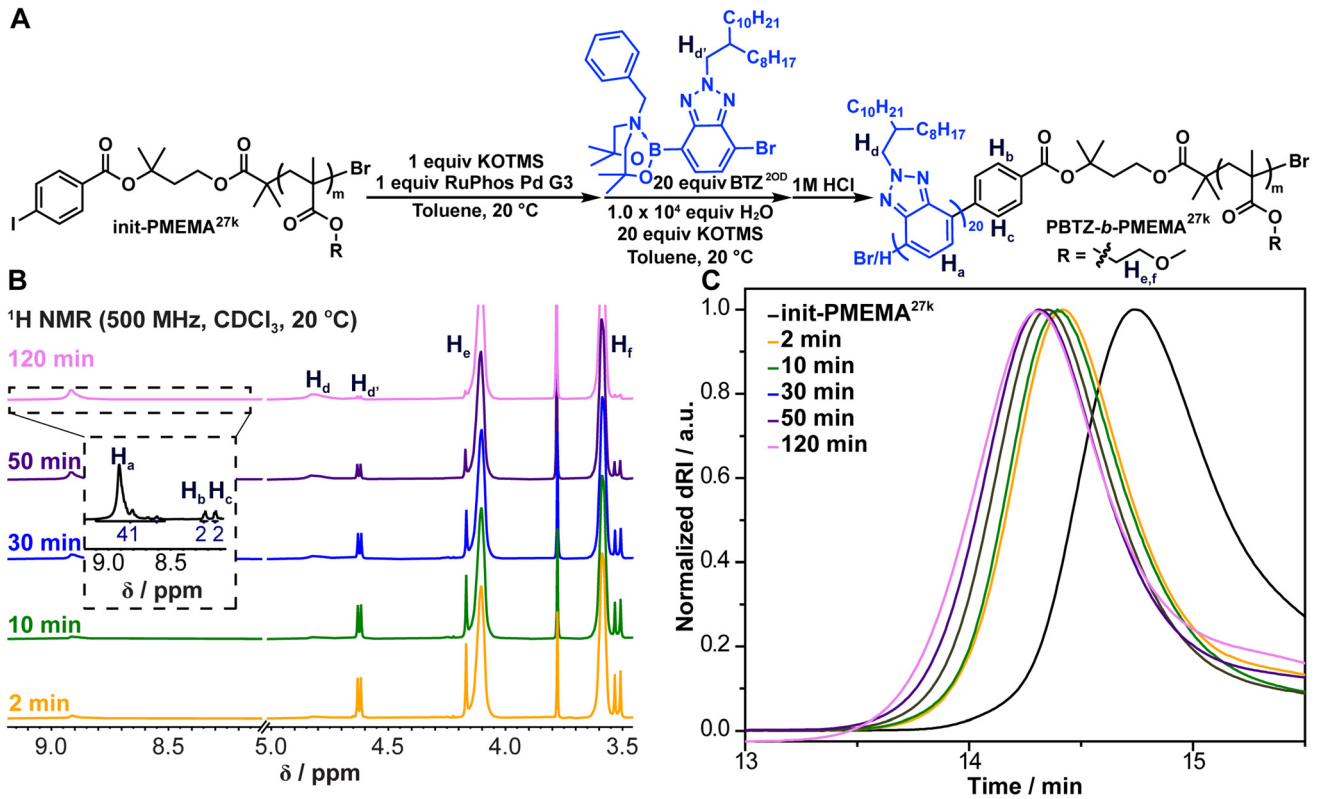

Fig. 3 (A) Chain extension of **init-PMEMA**^{27k} (entry 4 in Table 1) *via* SCTP to yield **PBTZ-*b*-PMEMA**. (B) Stacked ^{1}H NMR (500 MHz, $CDCl_3$, 23 °C) spectra of SCTP aliquots at different reaction times. (C) Normalized dRI traces of macroinitiator **init-PMEMA**^{27k} and its chain extension with **BTZ**^{2OD} at different reaction times.

Table 2 Library of **PBTZ-*b*-PRMAs** prepared in this study and utilized for solution self-assembly

Entry	Diblock copolymers[a]	f_{PBTZ} [b] (%)	$M_{n,NMR}$ [c] (kg mol^{-1})	$M_{n,GPC}$ [d] (kg mol^{-1})	$Đ$	Morphology[e]
1	**PBTZ$_{10}$-*b*-PMEMA$_{171}$**	16	29.0	25.7	1.04	Disordered lamellar
2	**PBTZ$_{22}$-*b*-PMEMA$_{251}$**	22	45.2	43.4	1.06	Toroidal
3	**PBTZ$_{24}$-*b*-PMEMA$_{265}$**	23	48.2	46.1	1.08	Toroidal
4	**PBTZ$_{15}$-*b*-PMEMA$_{58}$**	46	14.7	21.0	1.06	Lamellar
5	**PBTZ$_{14}$-*b*-PMEMA$_{34}$**	58	10.8	16.3	1.14	Lamellar
6	**PBTZ$_{43}$-*b*-PMEMA$_{46}$**	75	24.1	33.7	1.06	Toroidal
7	**PBTZ$_{50}$-*b*-PMEMA$_{30}$**	85	24.6	12.2	1.08	Toroidal
8	**PBTZ$_{77}$-*b*-PMEMA$_{29}$**	90	35.2	27.7	1.08	Vesicular/toroidal
9	**PBTZ$_{23}$-*b*-PDMA$_{187}$**	18	51.8	42.3	1.08	Toroidal
10	**PBTZ$_{14}$-*b*-PDMA$_{56}$**	31	18.6	21.0	1.08	Lamellar
11	**PBTZ$_{110}$-*b*-PDMA$_{57}$**	78	57.0	36.3	1.06	Nanofibers

[a] The values after the polymer block abbreviation represent the DP determined *via* ^{1}H NMR spectroscopy in $CDCl_3$. [b] f_{PBTZ} of PBZT in diblock copolymer. [c] M_n determined using ^{1}H NMR. [d] M_n and dispersity ($Đ$) determined using GPC-MALS in THF at 35 °C. [e] Morphology of the solution self-assembly observed *via* TEM.

the initiator from 0.8 mM to 0.4 mM allowed us to retain the solubility of the growing chains long enough to reach DPs up to 110 for the PBTZ block (Table 2, entries 6–8 and 11). Lastly, low values of $Đ$ (1.04–1.14) were observed, which is desirable for BCP self-assembly.[37] Following the outlined procedure, a library of **PBTZ-*b*-PMEMA**s and **PBTZ-*b*-PDMA**s was synthesized (Table 2). The GPC traces of entries in Table 2 before and after prep-GPC can be found in Fig. S3–S13. Molecular dynamics simulations (MD) were used to estimate the volume fraction of PBTZ (f_{PBTZ}) for each diblock copolymer shown in Table 2 (see SIMD).

Self-assembly of PBTZ-*b*-PRMAs

To understand the effects of the composition of the diblock copolymers on their solution-based self-assembly, we prepared a variety of solutions based on the solubility profiles of the diblock copolymers and observed the resulting particles *via* transmission electron microscopy (TEM). The room-tempera-

ture solubility profiles of the individual blocks are as follows: the PBTZ block is soluble in hexane (HXN) and tetrahydrofuran (THF) but not in ethyl acetate (EtOAc), the PMEMA block is soluble in THF and EtOAc but not in HXN, and the PDMA block is soluble in HXN, THF, and EtOAc.

All self-assemblies were carried out by dissolving the BCPs in THF to make a 1 mg mL^{-1} stock solution. A 0.1 mL aliquot of the stock solutions was placed into a separate vial equipped with a stir bar, to which 1 mL of ethyl acetate or hexane (EtOAc, HXN) was added dropwise while stirring (0.09 mg mL^{-1}) and the mixture was left to age at room temperature over the course of 2–7 days. In some cases, ill-defined aggregation of the BCPs was observed by TEM, which led us to increase the fraction of THF in the solvent mixture by adding an extra 0.1 mL of it to the 0.1 mL aliquot of the BCP stock solution prior to addition of EtOAc or HXN; this procedural modification slightly reduced the concentration of the BCPs to 0.08 mg mL^{-1}. A drop of the solution is placed upon a carbon-coated copper grid and used for TEM imaging without staining. Due to the electronic semi-conductive nature of PBTZ, the dark areas of the morphologies observed were attributed to self-assembled PBTZ. In what follows, the solution self-assemblies of **PBTZ-*b*-PMEMA** and **PBTZ-*b*-PDMA** are described in order of increasing f_{PBTZ}.

Self-assembly of PBTZ-*b*-PMEMA

The self-assembly of **$PBTZ_{24}$-*b*-$PMEMA_{265}$** (Table 2, entry 3) with 23% f_{PBTZ} was carried out in a 0.08 mg mL^{-1} solution with THF—a good solvent for both blocks—and EtOAc—a good solvent for PMEMA in a 0.1/1.0 v/v ratio. A five-day aging period resulted in round particles with diameters of 2.5 ± 1.3 μm (Fig. 4A). When the PBTZ-selective solvent system was used (0.1/1.0 v/v THF/HXN), a 48 hour aging period resulted in spherical particles that resemble large micelles or small vesicles and their aggregates (Fig. S14). A five-day aging period resulted in round particles with diameters of 0.9 ± 0.5 μm (Fig. 4B). Given their size, we hypothesized that these particles are vesicles or toroids in both cases, PBTZ selective solvent is about 3 times smaller than those formed using the PMEMA-selective solvent. We hypothesize that in HXN, the much longer PMEMA chains collapse to minimize their interaction with HXN and maximize that of PBTZ with HXN, leading to smaller particles compared to those formed using EtOAc (Fig. 4B).

The assembly of **$PBTZ_{14}$-*b*-$PMEMA_{34}$** (Table 2, entry 5) with f_{PBTZ} = 58% was carried out in a 0.09 mg mL^{-1} solution of 0.1/1.0 v/v THF/EtOAc and aged for 48 hours. TEM micrographs displayed what appeared to be disordered lamellae with an average PBTZ domain width of 6.9 ± 1.5 nm and PMEMA domain width of 6.8 ± 1.3 nm (Fig. 4C). The contour length of the **$PBTZ_{14}$** fragment is estimated to be 5.7 nm (see SI section Contour length), which suggests that the PBTZ chains are fully extended and interdigitated within their domains. When the solvent was changed to HXN, the average domain size for the PBTZ blocks was found to be 13.7 ± 1.9 nm, and that of the PMEMA—5.5 ± 1.5 nm. The average domain width of PBTZ is twice that observed in EtOAc, suggesting that the PBTZ domains incorporate two sets of non-interdigitated PBTZ blocks (Fig. 4C and D).[38]

To further probe our assignment of the lamellar morphology, a film of **$PBTZ_{14}$-*b*-$PMEMA_{34}$** was analyzed *via* small-angle X-ray scattering (SAXS) (Fig. 5). Admittedly, the morphology observed in the bulk need not be the same as under the dilute solution self-assembly conditions; however, we did utilize the same solvent ratios when drop-casting the BCP solutions to make the films for SAXS (see SI section Materials and methods). At room temperature, the diffractogram showed two broad peaks at 0.045 $Å^{-1}$ and 0.200 $Å^{-1}$, indicating a disordered morphology. When the sample was heated to 100 °C, the SAXS profiles revealed a sharpening and shift of the peak at 0.045 $Å^{-1}$ to 0.040 $Å^{-1}$ and the disappearance of the second peak (0.200 $Å^{-1}$). A further increase of the temperature to 140 °C, below the melting temperature, judging by the differential scanning calorimetry trace for a related BCP (Table 2, entry 1 and Fig. S15), led to a sharper peak at 0.040 $Å^{-1}$ and the appearance of a second order diffraction peak at 0.0811 $Å^{-1}$ that allowed us to assign a lamellar morphology for the BCPs in the bulk (Fig. 5). Small, medium, and wide AXS diffractograms of **$PBTZ_{14}$-*b*-$PMEMA_{34}$** can be found in Fig. S16. Again, although these results cannot be directly mapped onto the morphology we observe by TEM for **$PBTZ_{14}$-*b*-$PMEMA_{34}$** with f_{PBTZ} = 58%, it serves as indirect evidence for our assignment of the morphology in the TEM as disordered lamellae.

The self-assembly of **$PBTZ_{50}$-*b*-$PMEMA_{30}$** (Table 2, entry 7) with f_{PBTZ} = 85% was carried out in 0.1/1.0 v/v THF/EtOAc (0.09 mg mL^{-1}) and was left to age at room temperature over the course of 48 hours. The TEM micrographs of the self-assembly showed a bimodal distribution of round particles with average diameters of 94.7 ± 11.3 μm and 2.2 ± 1.0 μm in addition to spheroid aggregates with diameters of 292 ± 60 nm (Fig. 4E and Fig. S17), which we hypothesized above to be vesicles or toroids. For some particles, the assemblies of the BCPs at the interfaces appear to have been disrupted. Given the use of EtOAc, a poor solvent for PBTZ but a good one for PMEMA, we hypothesize that the vesicle walls or toroids are made of a bilayer of diblock copolymers with PBTZ in the center. We hypothesize that disruption of the vesicle wall or toroid is a result of the evaporation of EtOAc during sample preparation: as a result of the diminished interactions between the much smaller PMEMA blocks, the assembled structures are expected to be more susceptible to perforation under the sample preparation conditions and analysis by TEM, including application of a high vacuum. We attribute the absence of these disruptions for particles made *via* the self-assembly of **$PBTZ_{24}$-*b*-$PMEMA_{265}$** in EtOAc to the greater volume fraction of PMEMA, whose interactions serve to maintain the integrity of the spherical particles.

When **$PBTZ_{50}$-*b*-$PMEMA_{30}$** was assembled in 0.1/1.0 v/v THF/HXN (0.09 mg mL^{-1}), we again observed round particles —vesicles or toroids—with average diameters of 18.7 ± 9.4 μm (Fig. 4F), which is ~five times smaller than those formed in 0.1/1.0 v/v THF/EtOAc. We hypothesize that the PBTZ block

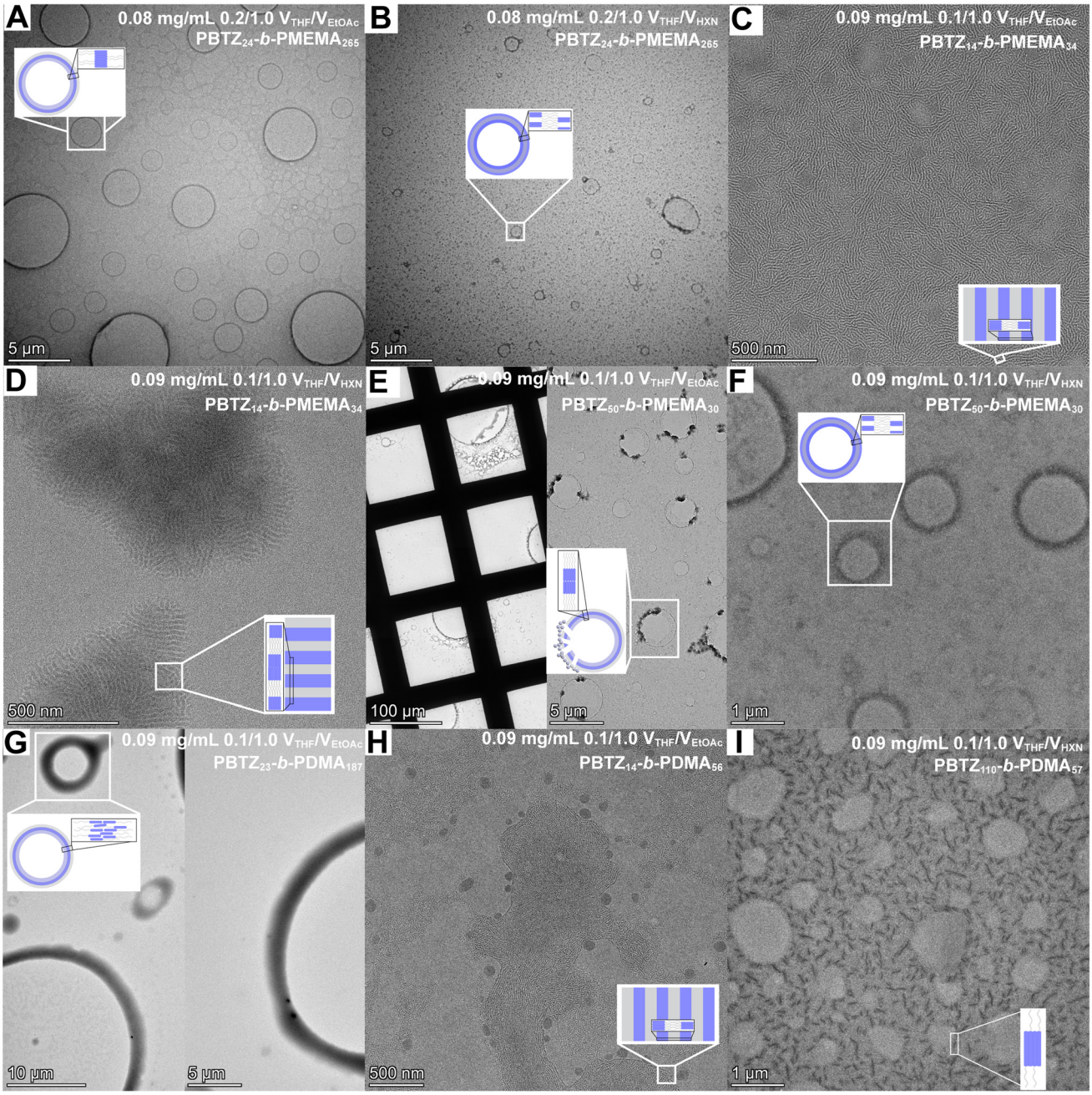

Fig. 4 (A)–(I) TEM micrographs of particles observed for (A) 0.08 mg mL^{-1} of **$PBTZ_{24}$-*b*-$PMEMA_{265}$** in 0.2/1.0 v/v THF/EtOAc, (B) 0.08 mg mL^{-1} of **$PBTZ_{24}$-*b*-$PMEMA_{265}$** in 0.2/1.0 v/v THF/HXN, (C) 0.09 mg mL^{-1} **$PBTZ_{14}$-*b*-$PMEMA_{34}$** in a solution of 0.1/1.0 v/v THF/EtOAc, (D) 0.09 mg mL^{-1} of **$PBTZ_{14}$-*b*-$PMEMA_{34}$** in 0.1/1.0 v/v THF/HXN, (E) 0.09 mg mL^{-1} of **$PBTZ_{50}$-*b*-$PMEMA_{30}$** in 0.1/1.0 v/v THF/EtOAc, (F) 0.09 mg mL^{-1} **$PBTZ_{50}$-*b*-$PMEMA_{30}$** in 0.1/1.0 v/v THF/HXN, (G) 0.09 mg mL^{-1} of **$PBTZ_{23}$-*b*-$PDMA_{187}$** in 0.1/1.0 v/v THF/EtOAc. (H) 0.09 mg mL^{-1} of **$PBTZ_{14}$-*b*-$PDMA_{56}$** in 0.1/1.0 v/v THF/EtOAc, and (I) 0.09 mg mL^{-1} of **$PBTZ_{110}$-*b*-$PDMA_{57}$** in 0.1/1.0 THF/HXN.

forms the outer layers of the particle to minimize the interactions between PMEMA and HXN, as previously observed for the self-assembly of **$PBTZ_{24}$-*b*-$PMEMA_{265}$**. Perforation of the particles was not observed for this assembly. We postulate that interactions such as π–π stacking between the much longer PBTZ blocks are strong enough to maintain the integrity of the particles after the evaporation of solvents. TEM micrographs of entries 1, 2, 4, 6 and 8 in Table 2 (Fig. S18–S22) display morphologies consistent with the trend of the representative samples presented above.

Self-assembly of PBTZ-*b*-PDMA

The assembly of **$PBTZ_{23}$-*b*-$PDMA_{187}$** (Table 2, entry 9, f_{PBTZ} = 18%) in 0.1/1.0 v/v THF/EtOAc (0.09 mg mL^{-1})—a good solvent for PDMA—resulted in particles that resemble toroids or vesicles with a bimodal average diameter of 35.9 ± 4.1 μm and 7.9

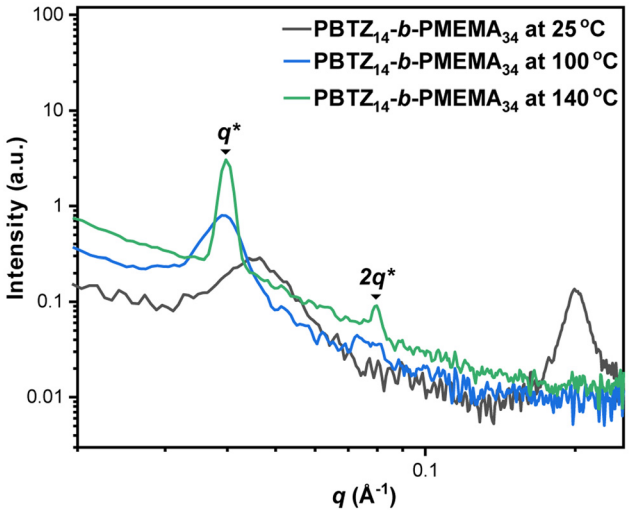

Fig. 5 SAXS diffractogram of $PBTZ_{14}$-*b*-$PMEMA_{34}$ film at 25, 100, and 140 °C.

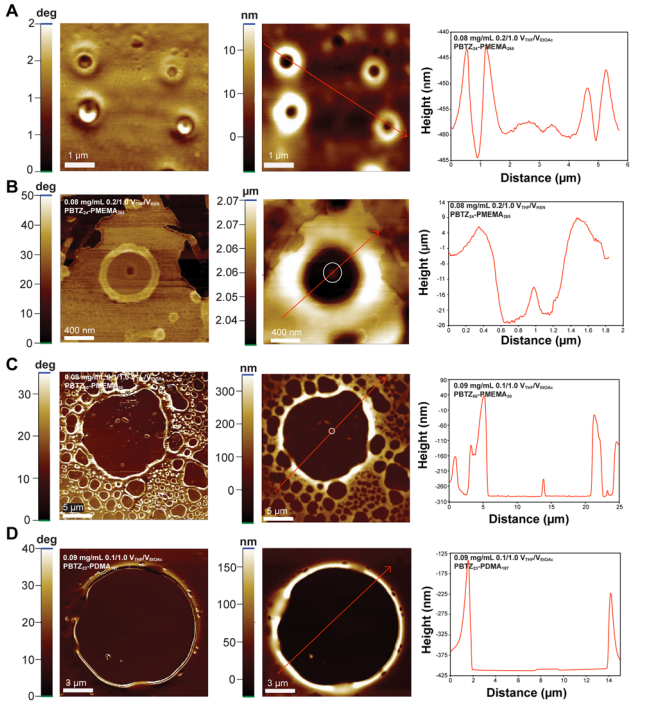

Fig. 6 (A)–(D) AFM phase image, height image, and height profile of (A) 0.08 mg mL^{-1} of $PBTZ_{24}$-*b*-$PMEMA_{265}$ in 0.2/1.0 v/v THF/EtOAc (B) 0.08 mg mL^{-1} of $PBTZ_{24}$-*b*-$PMEMA_{265}$ in 0.2/1.0 v/v THF/HXN, (C) 0.09 mg mL^{-1} of $PBTZ_{50}$-*b*-$PMEMA_{30}$ in 0.1/1.0 v/v THF/EtOAc, (D) 0.09 mg mL^{-1} of $PBTZ_{23}$-*b*-$PDMA_{187}$ in 0.1/1.0 v/v THF/EtOAc.

± 4.1 μm (Fig. 4G and Fig. S23). When a 0.09 mg mL^{-1} solution of $PBTZ_{14}$-*b*-$PDMA_{56}$ with f_{PBTZ} = 31% in THF/EtOAc (0.1/1.0 v/v) is assembled, we observe a mixture of spherical micelles with an average diameter of 84 ± 22 nm and lamellae with an average PBTZ domain width of 6.9 ± 1.1 nm and PDMA domain width of 5.8 ± 1.0 nm (Fig. 4H). The contour length of the fully stretched PBTZ block was estimated to be 5.9 nm, which suggests that the PBTZ chains are interdigitated.

The self-assembly of $PBTZ_{110}$-*b*-$PDMA_{57}$ with f_{PBTZ} = 78% was carried out at a concentration of 0.09 mg mL^{-1} in 0.1/1.0 v/v THF/HXN over a seven-day aging period to yield nanofibers with a length of 60 ± 20 nm and a width of 11 ± 2.5 nm (Fig. 4I). Based on the contour length of 45.8 nm calculated for the PBTZ block and the rigidity of this polymer core, we conclude that the PBTZ chains are likely arranged parallel to the long axis of the fiber, as indicated in the cartoon in Fig. 4I.

Atomic force microscopy analysis

To distinguish between the hypothesized vesicles and toroids in the assemblies described above, we elected to use atomic force microscopy (AFM). The assemblies were drop-cast onto silicon dioxide wafers, and AFM camera images of the assemblies were first collected to identify representative regions to be subjected to AFM (Fig. S24–S27). In the height images shown in Fig. 6, taller features appear lighter while shorter features appear darker.

The contrast in the phase image of $PBTZ_{24}$-*b*-$PMEMA_{265}$ (in 0.2/1.0 v/v THF/EtOAc) (Fig. 6A, left) shows round particles approximately 0.25 to 1 μm in outer diameter. The height image (Fig. 6A, middle) shows round particles with lighter/taller particle interfaces and darker/shorter centers. This topology is consistent with a toroidal morphology. The corresponding height profile (Fig. 6A, right) of the two toroids was used to estimate their inner diameter to be 0.7 μm with a thickness of approximately 0.2 μm for both toroids. Fig. 6B shows the phase image (left), height image (middle), and height profile (right) of a single particle from the assembly of $PBTZ_{24}$-*b*-$PMEMA_{265}$ (in 0.2/1.0 v/v THF/HXN). The phase image, height image, and height profile also suggest a toroidal morphology, analogous to those observed when the assembly was carried out in a THF/EtOAc solvent mixture. From the height profile, the width of the toroid is approximately 0.5 μm, and its inner diameter is approximately 1 μm. A change in topology seen in the height profile at 1 μm (white circle in height image) suggests the presence of a spherical particle with a diameter of approximately 7 nm, potentially formed *via* the aggregation of the BCPs. The AFM height and phase images of $PBTZ_{24}$-*b*-$PMEMA_{265}$ (in 0.2/1.0 v/v THF/EtOAc) (Fig. S28) also suggest a toroidal morphology.

The contrast in the phase images of $PBTZ_{50}$-*b*-$PMEMA_{30}$ (0.1/1.0 v/v THF/EtOAc) (Fig. 6C) displayed round particles analogous to those observed *via* TEM (Fig. 4E). Their corresponding AFM height images showed lighter/taller particle interfaces and dark/short centers, suggesting a toroidal morphology. Based on the height image and height profile, the thickness of the biggest toroid is approximately 2 μm with an inner diameter of approximately 16 μm. The increase in height at approximately 13.5 μm in the height profile suggests a change in topology, potentially due to the presence of a spherical particle with a diameter of approximately 60 nm (Fig. 6C, white circle).

The toroids appear to form a honeycomb framework, presumably *via* the aggregation of toroids of varying outer diameters. The disruption to the assemblies observed *via* TEM

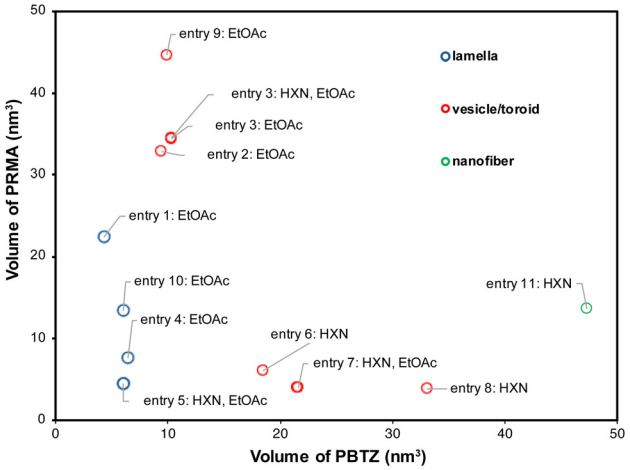

Fig. 7 Graph of the van der Waals volumes of PBTZ and PRMA on the *x*- and *y*-axes, respectively. Each data point is labeled with the entry number from Table 2 and the solvent added to THF.

was not seen *via* AFM. We speculate that a change in the substrate on which the assemblies were deposited—from a carbon-coated copper grid for TEM to a silicon dioxide wafer for AFM—paired with the honeycomb framework maintains the integrity of the toroids when characterized *via* AFM. Based on these data, we hypothesize that **PBTZ$_{50}$-*b*-PMEMA$_{30}$** also assembles in a THF/HXN solvent mixture (Fig. 4F) to form toroids.

A single particle made from the self-assembly of **PBTZ$_{23}$-*b*-PDMA$_{187}$** (0.1/1.0 v/v THF/EtOAc) was analyzed *via* AFM. The phase image (Fig. 6D, left), height image (Fig. 6D, middle), and height profile (Fig. 6D, right) were consistent with the topology of a toroid. The toroid has an approximated inner diameter of 10 μm—consistent with the range of particles observed *via* TEM for this assembly—and a thickness of approximately 0.5 μm.

To understand the experimental trends observed, we plotted the morphologies of the BCPs on a 2D plot with the MD simulation-derived volumes of PRMA and PBTZ on the *y*- and *x*-axes, respectively (Fig. 7, see SIMD). The clustering of the morphologies on this plot indicates that lower volumes of PBTZ favor the formation of a lamellar morphology, particularly at lower volumes of PRMA. Increasing the volume of PBTZ or PRMA blocks leads to toroidal particles, while if both are increased—particularly the PBTZ block—we observe the formation of nanofibers. Furthermore, while the solvent selectivity and identity of PRMA change the morphology observed, a change in volume fraction results in a morphological and topological change. Note that all morphology/particle imaging was carried out using drop-casting on surfaces, so solvent evaporation and chemistry of the surface could play a role in the observed particles. This question will be explored in future work.

Conclusions

To gain insight into the solution self-assembly of electron-deficient CPs, we synthesized a library of poly(benzotriazole)-*b*-poly(2-methoxyethyl methacrylate)s (**PBTZ-*b*-PMEMA**) and poly(benzotriazole)-*b*-poly(*n*-decyl methacrylate)s (**PBTZ-*b*-PDMA**) diblock copolymers with number average molecular weights ranging from 10.8 to 57.0 kg mol^{-1} and narrow molecular weight distributions ($Đ$ = 1.04–1.14). We studied their self-assemblies *via* TEM, SAXS, MD simulations, and AFM and delineated a trend in the formation of different morphologies—lamellae, toroids, and nanofibers—based on the volumes of the two blocks. Furthermore, we found that the solvent selectivity dictates the configuration of the BCPs in the particle walls. Notably, comparison of our self-assembly results to the most closely analogous study for a block-copolymer with a donor-type CP—namely poly(3-hexylthiophene)—reported by Lee and coworkers[33] reveals that our system behaves substantially differently: while they observed predominantly fibril-like or granular assemblies, our system displays an assortment of morphologies, including the rather unusual toroids. However, we cannot attribute with certainty this contrast to electronic differences between the CPs or differences in their geometric parameters, identity of the coil blocks, or other factors. This question would merit a follow-up study to be properly addressed. In short, this work paves the way for a broader elucidation of rod-coil BCP structure-solvent-morphology relationships with electron-deficient CP rod blocks.

Author contributions

A. V. Z. conceived and directed this work. A. V. Z., H. D. F., and L. J. designed the experiments, H. D. F. and L. J. carried out experiments, F. S. W. carried out MD calculations. E. C. K. helped with the acquisition and analysis of the X-ray scattering data. S. S. D. helped with AFM data acquisition and analysis. A. M. K. and M. N. J. assisted with experimental design and analysis for particle AFM characterization. The manuscript was written through the contributions of all authors. All authors have given approval to the final version of the manuscript.

Conflicts of interest

Authors declare no competing financial interest.

Data availability

The data supporting this article have been included as part of the SI. See DOI: https://doi.org/10.1039/d5py00773a.

Acknowledgements

We thank Renata Garces Perez (Department of Physics, Duke University) for help with X-ray scattering data collection.

This work was supported by DOD DAF Air Force Office of Scientific Research (AFOSR) Young Investigator Program

(FA9550-23-1-0083). Instrumentation utilized for data collection was supported by the National Science Foundation under Grant no. 1828183 (NMR instrument grant), Grant no. 0922858 (NMR instrument grant). TEM was performed in part at the Chapel Hill Analytical and Nanofabrication Laboratory, CHANL, a member of the North Carolina Research Triangle Nanotechnology Network, RTNN, which is supported by the National Science Foundation, Grant ECCS-1542015, as part of the National Nanotechnology Coordinated Infrastructure, NNCI. SAXS, MAXS, and WAXS measurements done at Duke University Shared Materials Instrumentation Facility (SMIF), a member of the North Carolina Research Triangle Nanotechnology Network (RTNN), which is supported by the National Science Foundation (award number ECCS-2025064) as part of the National Nanotechnology Coordinated Infrastructure (NNCI). National Science Foundation Grant no. 2443318 (AFM instrument).

References

1 C. K. Chiang, C. R. Fincher, Y. W. Park, A. J. Heeger, H. Shirakawa, E. J. Louis, S. C. Gau and A. G. MacDiarmid, *Phys. Rev. Lett.*, 1977, **39**, 1098–1101.
2 H. Shirakawa, E. J. Louis, A. G. MacDiarmid, C. K. Chiang and A. J. Heeger, *J. Chem. Soc., Chem. Commun.*, 1977, 578–580.
3 R. Salimian and C. Nardin, *Biomacromolecules*, 2023, **24**, 3411–3437.
4 B. Guo, Z. Sheng, D. Hu, A. Li, S. Xu, P. N. Manghnani, C. Liu, L. Guo, H. Zheng and B. Liu, *ACS Nano*, 2017, **11**, 10124–10134.
5 J. B. H. Tok and Z. Bao, *Sci. China: Chem.*, 2012, **55**, 718–725.
6 H. Dong and W. Hu, *Acc. Chem. Res.*, 2016, **49**, 2435–2443.
7 M. Pandey, N. Kumari, S. Nagamatsu and S. S. Pandey, *J. Mater. Chem. C*, 2019, **7**, 13323–13351.
8 O. Bubnova and X. Crispin, *Energy Environ. Sci.*, 2012, **5**, 9345–9362.
9 B. D. Olsen and R. A. Segalman, *Mater. Sci. Eng., R*, 2008, **62**, 37–66.
10 G. E. J. Hicks, S. Li, N. K. Obhi, C. N. Jarrett-Wilkins and D. S. Seferos, *Adv. Mater.*, 2021, **33**, 2006287.
11 L. R. MacFarlane, H. Shaikh, J. D. Garcia-Hernandez, M. Vespa, T. Fukui and I. Manners, *Nat. Rev. Mater.*, 2021, **6**, 7–26.
12 Z.-Q. Wu, D.-F. Liu, Y. Wang, N. Liu, J. Yin, Y.-Y. Zhu, L.-Z. Qiu and Y.-S. Ding, *Polym. Chem.*, 2013, **4**, 4588–4595.
13 S. Daripa, K. Khawas, A. Sharma, A. Kumar, B. Pal, S. Das, S. Jit and B. K. Kuila, *ACS Appl. Polym. Mater.*, 2020, **2**, 1283–1293.
14 F. Xu, J. Zhang, P. Zhang, X. Luan and Y. Mai, *Mater. Chem. Front.*, 2019, **3**, 2283–2307.
15 I. Geronimo, E. C. Lee, N. J. Singh and K. S. Kim, *J. Chem. Theory Comput.*, 2010, **6**, 1931–1934.
16 M. V. Bautista, A. J. Varni, J. Ayuso-Carrillo, C.-H. Tsai and K. J. T. Noonan, *ACS Macro Lett.*, 2020, **9**, 1357–1362.
17 J. Lee, H. Kim, H. Park, T. Kim, S.-H. Hwang, D. Seo, T. D. Chung and T.-L. Choi, *J. Am. Chem. Soc.*, 2021, **143**, 11180–11190.
18 H. Park, J. Lee, S.-H. Hwang, D. Kim, S. H. Hong and T.-L. Choi, *Macromolecules*, 2022, **55**, 3476–3483.
19 A. J. King and A. V. Zhukhovitskiy, *Angew. Chem., Int. Ed.*, 2022, **61**, e202206044.
20 P. Krys and K. Matyjaszewski, *Eur. Polym. J.*, 2017, **89**, 482–523.
21 K. Parkatzidis, H. S. Wang, N. P. Truong and A. Anastasaki, *Chem*, 2020, **6**, 1575–1588.
22 N. P. Truong, G. R. Jones, K. G. E. Bradford, D. Konkolewicz and A. Anastasaki, *Nat. Rev. Chem.*, 2021, **5**, 859–869.
23 A. Balan, G. Gunbas, A. Durmus and L. Toppare, *Chem. Mater.*, 2008, **20**, 7510–7513.
24 J. Cao, L. Wang, G. You, L. Li, L. Yao, Z. Zhou, E. Yang, W. Cai, Q. Ling and H. Zhen, *Dyes Pigm.*, 2022, **200**, 110170.
25 S. Yum, T. K. An, X. Wang, W. Lee, M. A. Uddin, Y. J. Kim, T. L. Nguyen, S. Xu, S. Hwang, C. E. Park and H. Y. Woo, *Chem. Mater.*, 2014, **26**, 2147–2154.
26 W. He, H. Jiang, L. Zhang, Z. Cheng and X. Zhu, *Polym. Chem.*, 2013, **4**, 2919–2938.
27 S. Harrisson, R. Whitfield, A. Anastasaki and K. Matyjaszewski, *Nat. Rev. Methods Primers*, 2025, **5**, 2.
28 Z. Gu, Y. Tan, K. Tsuchiya, T. Shimomura and K. Ogino, *Polymers*, 2011, **3**, 558–570.
29 E. Kaul, V. Senkovskyy, R. Tkachov, V. Bocharova, H. Komber, M. Stamm and A. Kiriy, *Macromolecules*, 2010, **43**, 77–81.
30 S. Fujiki, K. Amaike, A. Yagi and K. Itami, *Nat. Commun.*, 2022, **13**, 5358.
31 M. Charton, *J. Am. Chem. Soc.*, 1975, **97**, 3691–3693.
32 J. Stejskal, J. Janca and P. Kratochvíl, *Polym. J.*, 1976, **8**, 549–555.
33 H.-N. Choi, H.-S. Yang, S. Park, T.-L. Choi and I.-H. Lee, *Macromolecules*, 2024, **57**, 8050–8058.
34 C. P. Delaney, D. P. Marron, A. S. Shved, R. N. Zare, R. M. Waymouth and S. E. Denmark, *J. Am. Chem. Soc.*, 2022, **144**, 4345–4364.
35 H. Xiong, Q. Lin, Y. Lu, D. Zheng, Y. Li, S. Wang, W. Xie, C. Li, X. Zhang, Y. Lin, Z.-X. Wang, Q. Shi, T. J. Marks and H. Huang, *Nat. Mater.*, 2024, **23**, 695–702.
36 M. V. Bautista, A. J. Varni, J. Ayuso-Carrillo, M. C. Carson and K. J. T. Noonan, *Polym. Chem.*, 2021, **12**, 1404–1414.
37 K. E. B. Doncom, L. D. Blackman, D. B. Wright, M. I. Gibson and R. K. O'Reilly, *Chem. Soc. Rev.*, 2017, **46**, 4119–4134.
38 M. Lee, B.-K. Cho and W.-C. Zin, *Chem. Rev.*, 2001, **101**, 3869–3892.

